Invited paper on EMRS Spring Meeting 2001, to appear in Computational Materials Science

PAPER REFERENCE: A-II.1

MULTISCALE APPROACHES FOR METAL THIN FILM GROWTH

P. Vogl,[1]* U. Hansen[1], V. Fiorentini[2]

[1]Walter Schottky Institute, Technische Universität München,
Garching, D-85748, Germany
[2]Istituto Nazionale per la Fisica della Materia
and Dipartimento di Fisica, Università di Cagliari, Italy

Abstract

Two recently developed multiscale approaches for simulations of metalization morphologies under ionized sputter deposition conditions are reviewed. These methods are capable of predicting the growth of thin films on the feature scale, based on calculations that are simultaneously carried out on all relevant scales and consistently employ data from atomistic simulations. In both techniques, the first step consists in molecular dynamics simulations that compute the relative probabilities of all relevant reactions taking place during physical vapor deposition. These probabilities are consequently employed in feature-scale simulators. One of the methods employs a 2-dimensional cellular-automaton technique to calculate the film topographies. The second approach employs a Green function method to combine the molecular dynamics results with a line of sight transport model in a 2-dimensional feature, and incorporates all effects of re-emission and re-sputtering in a

* Corresponding Author: Tel. +49 89 289 12750; Fax. +49 89 289 12737; E-mail: vogl@wsi.tum.de

self-consistent manner. In the final step, a level-set method is used to describe the morphology of the growing film. Both methods provide complete growth rate models that allow the inclusion of energy and angular dependent reaction rates. Several applications of both techniques are discussed.

Keywords: Multiscale model, film growth, vapor deposition

1. Introduction

Vapor deposition is a widely used process to create thin films and coatings for many applications, such as the metalization of semiconductor wafers or production of magnetic layers [1,2]. Because of the complexity of vapor deposition, increasing reliance is placed upon modeling. Since vapor deposition is a multiscale process that intimately couples atomic scales (10^{-13} m and 10^{-16} s) with macroscopic reactor scales (1m and 10^2 s), a predictive modeling of vapor deposition is a challenging problem that requires multiscale models that are capable of spanning those many time and length scales [3,4].

Fortunately, the ability to study, check and verify in-situ or ex-situ growth processes experimentally with atomic resolution, together with the availability of powerful computers, has led to enormous progress in multiscale modeling recently, and quite a number of excellent reviews is available that provide a timely overview of the state-of-the-art [5-8].

Current simulation techniques can be roughly grouped into three classes: (i) Density functional calculations or molecular dynamics simulations start from atomistic scales and attempt to extend

their scope - with increasing complexity and cost - to sub-mesoscopic scales [9,10]. (ii) Hybrid continuum models such as level set techniques [11] calculate growth fronts, the time evolution of step edges, or dislocations on a macroscopic scale based on differential equations in configuration space. By using parameters from experiment as well as from microscopic simulations, these models have shown remarkable success down to mesoscopic scales [6]. (iii) Lattice Monte-Carlo methods for mesoscopic film scale simulations have been devised that can, in principle, span all relevant time and length scales of vapor deposition including the sputtering process in physical vapor deposition, provided the number of competing growth processes is limited and their rates are known [12,13]. This method is also very promising but as yet less suited for the study of lattice-misaligned effects such as grain boundaries or high energy deposition processes that generate lattice defects.

This discussion indicates that methods that link the continuum and Monte-Carlo methods to atomic scale simulations in a consistent manner are just emerging [5,6,14]. While the gaps between the methods of type (1) to (3) are becoming smaller, more work is needed to provide a glue between the different scales, and develop models that are able to truly cross length and time scales by using microscopic results as input and produce results on a macroscopic scale without further empirical intervention and, ideally, without loss of accuracy.

In this paper we shall review two predictive simulation techniques for ionized physical vapor deposition (IPVD) that belong to the latter class, and are thus capable of predicting the growth of thin films on the feature scale, based on calculations that are simultaneously carried out on all relevant scales [15-17]. These approaches employ data from atomistic simulations (i.e. angular and energy dependent surface reactions rates) that get coarsened in a systematic fashion so as to finally

predict growth fronts on the wafer scale. The IPVD process is becoming increasingly relevant for filling deep trenches with large aspect ratios depth/width on semiconductor wafers [18,19]. It is based on in-flight ionization of atoms sputtered from a target and yields impinging energies of the ions that are typically of the order of 100 eV.

Naively, one might expect that it is simpler to model growth processes that occur close to equilibrium (such as molecular beam epitaxy or chemical vapor deposition where the deposited atoms have a kinetic energy of 0.1 to 1 eV) rather than processes that are very far from equilibrium. Indeed, a characteristic of IPVD is not only the high growth rate of the order of 40 monolayers/sec [20,21], but the fact that several competing processes such as sputtering, absorption, and emission occur with roughly equal probabilities and need to be accurately taken into account.

Nevertheless, the high energy of the impinging atoms is also the key that allows one to simplify the development of predictive feature scale models for IPVD significantly: The detailed surface morphology becomes less relevant, at least for the commonly used metals such as Al, Cu, Ti, and Ta [15-17]. The high flux rate and high energy bombardment of the surface just allows for sufficient healing between impacts that the surface does not become amorphous, but long range spatial correlations and surface diffusion processes are suppressed or at least impeded. The film growth becomes dominantly columnar rather than diffusion-controlled [22,23]. Importantly, experimental SEM data (such as will be discussed below, see Figure 7) exhibit sharp cusps and roof-like structures that would be smoothened out if mesoscopic diffusion played a determining role. Consequently, it is the geometry of the feature on a mesoscopic scale rather than microscopic processes that lead to spatially varying growth rates. In other words, growth processes that lie mesoscopic

distances apart from each other can be treated as independent. This key property allows one to design growth models that consistently span all relevant scales.

We begin by reviewing a molecular dynamics based growth rate model, and combine it with a cellular automaton and with a line of sight transport model within the feature, respectively, to predict growth fronts on the feature scale [15]. The resulting deposition models can account for arbitrary angular and energetic dependence of surface reaction rates and include all effects of re-emission and re-deposition.

2. Reaction rates from molecular dynamics

IPVD is based on in-flight ionization of atoms sputtered from a target. The metal atoms knocked out of the target by argon ions experience ionization as they pass through a high density plasma generated by a radio frequency antenna before reaching the substrate. The electric field at the biased substrate tends to collimate this metal ion flux [19]. Using data from molecular dynamics simulations in growth modeling [3,4,10,14,15,24-26] is an approach clearly superior to other simplified models which employ energy and angular independent rate constants instead.

We have performed classical molecular dynamics simulations [10,27] for the Al system using an extensively tested embedded atom type [28,29] potential for the Al-Al interaction [30,31]. Details of the molecular dynamics simulations are described in our previous work, see Refs. [15-17]. Under non-thermal deposition conditions, the key physical surface processes can be classified as adsorption, reflection and sputtering events, i.e. the removal of surface atoms and adsorbates by the

impact of energetic particles. The relative probabilities for the surface reactions are defined as the ratio of the number of events of each kind to the total number of trajectories. In the following we discuss the energy and angular dependence of the relative probabilities of these processes [16].

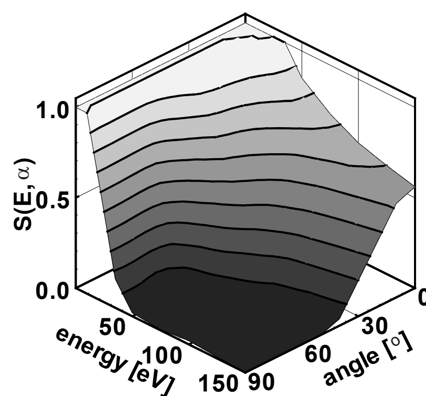

Fig. 1. Calculated sticking probabilities for hyper-thermal Al atoms impinging on an Al(111) surface as a function of the incident kinetic energy and off-normal angle α. The surface temperature was set to 450 K, i.e. about half the melting temperature. The contour lines mark increments of 0.1 in the sticking probability

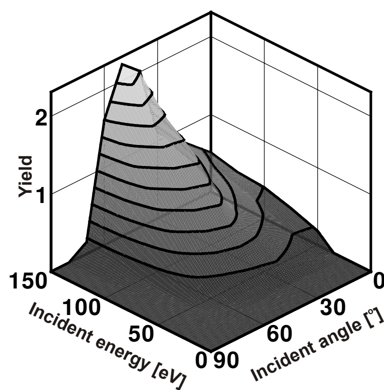

Fig. 2. Calculated sputter yield, i.e. number of particles leaving the surface divided by the number of particles impinging on the surface, for hyper-thermal Al atoms impinging on an Al(111) surface as a function of kinetic energy and off-normal angle α. The surface temperature was set to 450 K. The contour lines mark increments of 0.2 in the yield.

For low energies (characteristic for molecular beam epitaxy) all Al atoms are adsorbed independent of their impact angle. If the incident kinetic energy is increased the situation completely changes and the sticking probability becomes strongly energy and angle dependent (Figure 1). High energies and large off-normal angles cause all particles to be reflected, hence the adsorption probability drops to zero.

During the sputter process not only single particles are etched away from the surface so that the yield, i.e. the number of particles leaving the surface divided by the number of particles impinging on the surface is obtained by multiplying the sputter probability by the actual multiplicity for the event (Figure 2). The etch yield reaches a pronounced maximum for angles around 50° and decreases near grazing angles. There is a preferred direction for the sputtered particles, which depends on the underlying crystal structure and surface orientation [see [17] for details].

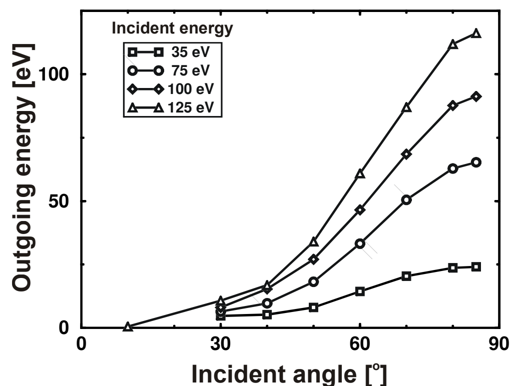

Fig. 3. Calculated final mean kinetic energy of hyper-thermal Al atoms being reflected from the Al(111) surface as a function of their incident off-normal angle and energy. The open squares, circles, diamonds and triangles correspond to incident energies of 35, 75, 100 and 125 eV respectively. The surface temperature was set to 450 K.

For incident energies in the range between 35 and 125 eV and off-normal angles between 10° and 85°, Figure 3 shows the mean kinetic energy for particles being reflected from the surface. With increasing angle we find a transition from diffuse to specular reflection events [17].

2.1 Surface roughness

So far, we have tacitly assumed an ideal Al (111) surface, a condition that is certainly not realistic for the high energy ion bombardment of the surface that is happening in IPVD. It is therefore relevant to compare an ideal surface with a “worst case” configuration in the sense of a very rough surface [17]. The first configuration that we have chosen is a flat Al(111) surface and the second surface a highly stepped Al(211) surface (see Figure 4). An impinging particle on a surface subject to sputter conditions probably experiences an average surface morphology that will be something in between the latter two extreme cases.

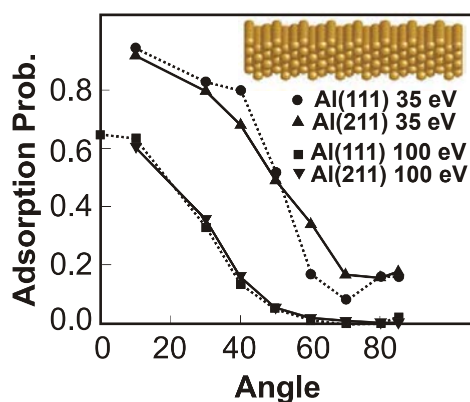

Fig. 4. Absorption probability of Al atoms on a flat Al(111) and stepped Al(211) surface, respectively, calculated with molecular dynamics [17] for 2 different incident kinetic energies as a function of the incident angle. The inset depicts an Al(211) surface.

We have determined the probability of adsorption, reflection, and etching as a function of the energy and off-normal angle of incident Al atoms for both types of surfaces [15,17]. For kinetic energies of about 100 eV we observe nearly identical reaction rates as is exemplified in Figure 5 for the sticking probability. For smaller energies of about 35 eV, we do observe some minor differences which are related to a slightly higher sputtering yield at medium angle of incidence and to scattering of the incident particles at step edges for grazing incidence. Nevertheless, the overall finding is that, fortunately, the reaction rates are insensitive to surface roughness for the relevant ion energy ranges in the IPVD process.

3. Feature-scale cellular automaton simulator

In this section we discuss a two-dimensional cellular automaton (CA) to model the growing Al film front on a μm scale [15]. The automaton accounts for the effects of flux shadowing, adsorption, reflection, etching, and surface diffusion. The simulated structure is represented in cross section by a two-dimensional grid. Each grid cell represents an Al atom, and is assumed to have a physical length of 2.5 Å, (the effective atomic diameter in Al bulk): thus, for example, a 1 μm wide structure will be described by 4000 grid cells across [15].

The atoms are serially and independently emitted from the sputter source far above the surface according to a pre-determined angular and energetic distribution, and move on a straight trajectory, determined also by the applied source-target bias, until they strike the growing film front. Interactions in the gas phase are neglected in view of the low pressure (typically a few tenths of

mTorr) and the resulting long mean free path typical of sputter deposition. Spontaneous desorption is also negligible in all the conditions considered.

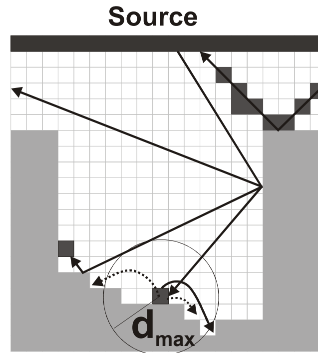

Fig. 5. Schematic picture of cellular automaton. The deposited particles are shown in black, and the trajectories shown are typical reflection, adsorption, and etching processes. The adsorption is connected to a diffusion process within length $d_{\max}$ that ends in a position that maximizes the number of nearest neighbors.

The impact angle and energy of the atoms hitting the surface determine which process is activated upon impact. This may be any one of the three (adsorption, reflection, etching) whose relative probabilities have been previously calculated via the MD simulations that we summarized in the previous section. If the atoms are reflected, or an etch process takes place, the path of the corresponding atoms is further traced until they hit the film surface for a second time. The three basic processes can then take place again, and so forth. Finally, the atoms get either adsorbed, or escape back into the gas phase. Figure 5 provides a schematic picture of some trajectories that are mapped onto this discrete system [15]. Care must be taken in mapping the continuous motion of the particles onto the CA. To give an example, the surface normal at a particular surface point must calculated from the center of mass of all particles lying within some chosen radius around that point. in order to maintain sufficient angular resolution in the simulation. The model aims at maxi-

mizing the coordination of the new particle, with the constraint that the impact-to-final site distance is minimized (so that the local film curvature is minimized [32] and the energy be minimized [33]).

3.1 Cellular automaton results of topography simulations

Figure 6 depicts trench topographies predicted by the CA model for different deposition conditions, compared to scanning-electron-microscope (SEM) pictures taken in similar conditions [20]. The structure size is 1.2 μm across. In the cellular automaton simulation, the emitted atom energies are picked from a Thompson distribution centered at 3 eV, as suggested experimentally. [21,34] The initial angles of the non-ionized atoms are chosen from a collimated cosine distribution with a maximum off-normal angle of 40°. To mimic the experimental conditions, we assume that 80 % of the emitted Al atoms get one-fold ionized; for these atoms, the trajectory and impact energy change according to the applied source-target bias.

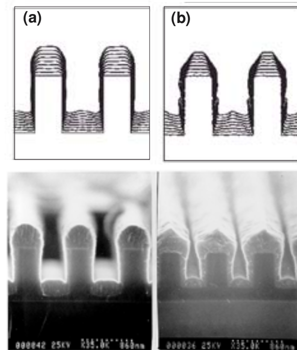

Fig. 6. Film morphologies on trench structures predicted [15] for different ionized magnetron sputtering conditions compared to experiments [20]. In panel (a) we assumed 80 % ionization, and 10 V bias, in panel (b) 80 % ionization, and 80 V bias. The material deposited in the simulations (a) and (b) corresponds to a total number of 16×10^{6} atoms. Below, a SEM micrograph with experimental results [20] is shown.

The results indicate that, depending on the sputter source-to-target bias, there are two regimes that correspond to the low and high energy regimes identified in our MD calculations (cf. Figs. 1, 2). The simulations in panel (a) of Fig. 6 were obtained by setting the bias equal to 10 eV. In agreement with experiment (also displayed in Fig. 6), the calculations predict a film growth front of rounded shape on top of the feature and, due to geometric shadowing, a reduced film thickness at the bottom of the trench. The pile-up at the center of the trench is not only of geometric origin, but also partly due to reflections of atoms impinging on the trench sidewalls. In panel (b) of Fig. 6, we show results obtained with a bias of 80 eV. The calculations predict, in accord with experiment, a roof-like structure on top of the feature. This structure is due to the preferential etching at angles of 50^0 (see Fig. 2) which leads to a lower deposition rate on the roof-like structure.

4. Self-consistent Green function method for metal film topographies

Recently, we have proposed another computationally efficient scheme to model the growth of thin films under IPVD conditions [16]. It uses a Green function approach that allows one to accurately employ data from atomistic simulations (i.e. angular and energy dependent surface reactions rates) within the level-set method [11]. Furthermore all effects of re-emissions are included so that one arrives at a model that provides a great speed advantage compared to Monte Carlo methods while retaining the accuracy of an atomistic approach, and easily resolving problems with low growth rates.

The basic idea of the method is to summarize the atomistic MD results in a fashion that is readily compatible with a species transport model [16]. Given an incident vector flux, $\Phi^{in}(E^{in},\theta^{in})$, at a particular energy E^{in} and angle θ^{in}, a Green function $G_i(E^{in},\theta^{in} \rightarrow E^{out},\theta^{out})$ that summarizes all the surface events is used to relate the emitted and incident fluxes in a manner consistent with the pre-tabulated MD results for atoms of type *i*. The re-emitted flux $\Phi_i^{out}(\mathbf{r},E',\theta')$ can be determined by the equation

$$\Phi_i^{out}(\mathbf{r},E',\theta') = \int_0^{\infty} dE \int_{-\pi/2}^{\pi/2} d\theta \, G_i(E,\theta \rightarrow E',\theta') \, \Phi_i^{in}(\mathbf{r},E,\theta) \tag{1}$$

Within the context of the feature scale model, material arriving from the reactor chamber may be treated as arriving from a source above the substrate surface. The flux from the source of each species, and its angular and energy distribution are specified as inputs to the model. After leaving the source, the impinging particles can experience three possible surface reactions, namely adsorption, sputtering and reflection, according to the previously discussed MD results.

Let us assume that a highly energized particle or ion hits the surface at a point **r,** looses part of its kinetic energy, and gets reflected. Then it can subsequently hit another piece of the surface **r'**, and gets either adsorbed or again reflected, etc. In such a scenario the point **r'** will act as an additional source. For a typical trench profile these two contributions are illustrated in Figure 7 (a). For some chosen point **r** at the sidewall, it depicts the range of incident impact angles for the direct flux. The arrow indicates the direction of a source particle, the dark grey area marks the angular range of all source particles contributing to the influx at position **r**. In Figure 7 (b), the origin of the re-emitted flux arriving at **r** is shown. Now the flux is arriving from other points along the surface and the

gray area marks those points, that can be ``seen" by **r**. Both contributions have to be considered for an accurate description of the front velocity at **r**.

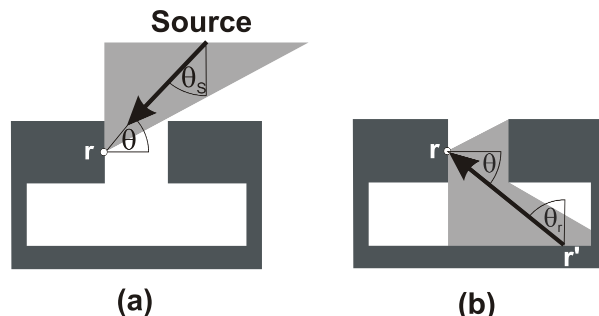

Fig. 7. Self-consistent Green function scheme for trench profile. (a) depicts for point **r** the so-called direct flux, i.e. the flux from the source that can reach this point. (b) illustrates the contribution from the re-emitted flux at **r** due to particles that have been reflected or etched away from **r**'. The arrows indicate the directions the material stems from. The dark shaded areas mark the angular range of the incoming flux.

Thus, in every system with micro-scale topography, a non unity sticking coefficient and/or a non-vanishing probability for re-sputtering implies that the total arriving flux stems from two possible reactions. The first one is the direct flux, i.e. the flux of atoms that leave the source and arrive at the surface before contacting another part of the feature. The second source of material is the flux due to re-emissions, which stems from reflection and sputtering events.

In addition to metal atoms arriving from the source *S* during IPVD growth, there will also be a significant flux of rare-gas ions, such as Ar^+. The source *S* emits each species *i* with the angular and energy dependent vector flux density $\Phi_i^S(E,\theta_S)$ where *E* is the energy of the released particle, θ_S is the off-normal angle with respect to the normal of the source plane and *i* is an index that describes the type of emitted particle (i.e. metal 1, metal 2, ..., rare-gas 1, rare-gas 2 , ...). Knowing the fluxes

from the source, the feature geometry, and the Green function G from Eq. (1), the incident flux of each species i at any point $\mathbf{r}$, on the feature surface can be written as [16]:

$$\Phi_i^{in}(\mathbf{r}, E, \theta) = \Phi_i^{source}(E, \theta_S) + \Phi_i^{out}(\mathbf{r}', E, \theta_R(\mathbf{r}')) \tag{2}$$

The first term on the right represents the direct flux, the second represents the flux re-emitted from other points $\mathbf{r}$' of the feature surface. The ray joining emitting points $\mathbf{r}$' with receiving point $\mathbf{r}$, makes angle θ with the receiving surface normal, and angle θ_R with the normal of the emitting surface. Equation (1) and (3) must now be solved self-consistently by an iterative scheme[16].

Once the front velocity has been calculated, we have employed the level-set method [35,11] to trace the shape of the moving boundaries in time. The level-set method avoids the shortcomings of other front tracking algorithms and offers a highly robust and accurate state of the art technique for tracking interfaces that works very well in any number of space dimensions [36].

4.2 Comparison of PVD and IPVD growth

As an application of the self-consistent Green function method, we take a closer look at the differences of the film topographies deposited under PVD and IPVD conditions. During conventional PVD sputtering, the angular and energetic distributions are well described by Thompson distributions [16,21,37]. Most of the atoms have rather low energies so that reflections and re-sputtering from the surface are negligible. For ionized physical vapor deposition, on the other hand, the situation completely changes. The metal atoms are knocked out of the source by

argon ions and experience ionization as they pass through a high density plasma generated by a radio frequency antenna before reaching the substrate. The electric field at the biased substrate highly collimates the ions and accelerates them, giving an energetic distribution that is shifted to much higher energies [38].

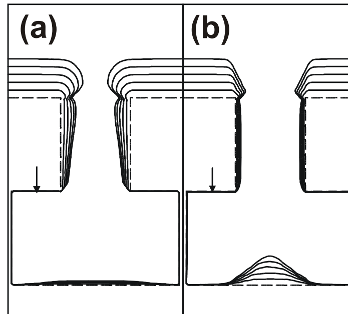

Fig. 8. Simulated thin film topographies under different deposition conditions for an undercut structure with an width of 0.2 μm at the opening and 0.4 μm at the undercut. In panel (a) an Al film under PVD conditions is deposited. In (b) 80 % of the incoming Al flux is ionized and modeled by a highly collimated angular distribution. The arrows mark positions geometrically shadowed from the source. The film thicknesses at these points amount to 0Å and 20 Å for (a) and (b), respectively.

Fig. 8 shows a comparison of metal thin films deposited under PVD (a) and IPVD (b) conditions, as calculated by the Green function method [16]. The panel (a) of Fig. 8 shows the thin film topographies deposited with PVD on a trench with an undercut structure. The solid contour lines show the evolving film front at constant time intervals, the dashed lines depict the initial geometry before the metal deposition. Most particles are adsorbed when they hit the trench sidewall thus leading to a buildup of material at the opening that shadows the bottom regions.

For an IPVD source, we show the film fronts at different stages of growth in Fig. 8 (b). To allow a qualitative comparison between the different deposition conditions, the front velocity was scaled such that the growth rates on the flat surfaces were the same in the PVD and IPVD case [panels (a) and (b) respectively]. Re-sputtering processes from the large deposit at the feature bottom greatly improves the sidewall coverage and deposition at those parts of the undercut structure that are geometrically shadowed from the source. The pile up of material at the bottom is beveled towards the edges due to the maximum in the etch rate at angles around 45° (see Fig. 3).

In summary, we have presented two efficient multiscale approaches to implement angular and energy dependent surface reaction rates that are relevant for ionized physical vapor deposition (IPVD) of thin metallic films. The methods discussed here capture the major differences between IPVD and standard PVD deposition and display the strengths of deposition with high energy ions, namely a more conformal sidewall coverage and a better bottom coverage.

Acknowledgments

We thank Dr. Alfred Kersch for helpful discussions and valuable guidance throughout the project. Financial support by the Office of Naval Research under Contract No. N00014-01-1-0242, the Infineon AG and the Deutsche Forschungs-Gemeinschaft under SFB 348 is greatfully acknowledged. One of us (V.F.) acknowledges support by the Alexander von Humboldt Foundation.

References

[1] S. M. Rossnagel, IBM J. Res. Dev. 43 (1999) 163.

[2] M. K. Sheergar, T. D. Smy, S. K. Dew, M. J. Brett, J. Vac. Sci. Technol. B 14 (1996) 2595.

[3] J. Dabrowski, H.-J. Müssig, M. Duane, S.T. Dunham, R. Goossens, H.-H. Vuong, Advances in Solid State Physics 38 (1998) 595.

[4] A. F. Voter, in: Interatomic Potentials for Atomistic Simulations, MRS Bulletin 21 (1996) 17.

[5] H. N. G. Wadley, X. Zhou, R. A. Johnson, M. Neurock, Prog. Mater. Sci. 46 (2001) 329.

[6] F.H. Baumann, D.L. Chopp, T. Díaz de la Rubia, G.H. Gilmer, J.E. Greene, H. Huang, S.Kodambaka, P. O'Sullivan, I.Petrov, MRS Bulletin, March 2001, p. 182.

[7] G. B. Olson, Science 277 (1997) 1237.

[8] K. Ohno, K. Esfarjani, Y. Kawazoe, Computational Materials Science, Springer, Berlin, 1999.

[9] R.Stumpf, M. Scheffler, Phys.Rev.B 53 (1996) 4958.

[10] D. Frenkel, B. Smit, Understanding Molecular Simulations: From Algorithms to Applications, Academic Press, Boston, 1996.

[11] J. A. Sethian, Level Set Methods and Fast Marching Methods, Cambridge University Press, Cambridge, 1999.

[12] C. Huang, G. H. Gilmer, T. D. de la Rubia, J. Appl. Phys. 84 (1998) 3636.

[13] G.H. Gilmer, H.C. Huang, T. Diaz de la Rubia, F.H. Baumann, J. Dalla Torre, Thin Solid Films 365 (2000) 189.

[14] X. W. Zhou, H. N. G. Wadley, Acta Mater. 47 (1999) 1063.

[15] U. Hansen, P. Vogl, V. Fiorentini, Phys. Rev. B 59 (1999) R7856.

[16] U. Hansen, S. Rodgers, K. F. Jensen, Phys. Rev. B 62 (2000) 2869.

[17] U. Hansen, A. Kersch, Phys. Rev. B 60 (1999) 14417.

[18] F. Cerio, J. Drewery, E. Huang, G. Reynolds, J. Vac. Sci. Technol. A 16 (1999) 1863.

[19] Z. C. Lum, J. E. Forster, T. G. Snodgrass, J. H. Booske, A. E. Wendt, J. Vac. Sci. Technol. A 17 (1999) 840.

[20] S. Hamaguchi, S. M. Rossnagel, J. Vac. Sci. Technol. B 13 (1995) 183.

[21] W. D. Westwood, in: Microelectronic Materials and Processes, R. A. Levy (Ed.), Kluwer, Dordrecht, 1989, p.133.

[22] C. R. M. Grovenor, H. T. G. Hentzell, D. A. Smith, Acta Metall. 32 (1984) 773.

[23] W. C. Liu, CH Woo, Hanchen Huang, J. Computer-Aided Mat. Design 6 (1999) 311.

[24] X. W. Zhoua, H. N. G. Wadley, Surf. Sci. 431 (1999) 42.

[25] D. E. Hanson, A. F. Voter, J. D. Kress, J. Appl. Phys. 82 (1997) 3552.

[26] D. G. Coronell, D. E. Hanson, A. F. Voter, C. L. Liu and J. D. Kress, Appl. Phys. Lett. 73 (1998) 3860.

[27] M. P. Allen, D. J. Tildesley, Computer Simulation of Liquids, Oxford University Press, Oxford, 1996.

[28] M. S. Daw, M. I. Baskes, Phys. Rev. B 29 (1984) 6443.

[29] M. S. Daw, M. I. Baskes, Phys. Rev. Lett. 50 (1983) 1285.

[30] F. Ercolessi, J. B. Adams, Europhys. Lett. 26 (1994) 583; U. Hansen, P. Vogl, V. Fiorentini, Phys. Rev. B 60 (1999) 5055.

[31] A. A. Abrahamson, Phys. Rev. 178 (1969) 178.

[32] S. K. Dew, T. Smy, M. J. Brett, IEEE Trans. Electron. Dev. 39 (1992) 1599.

[33] M. Methfessel, D. Hennig, M. Scheffler, Appl. Phys. A 55 (1995) 442.

[34] E. Dullini, Nucl. Instr. and Meth. B 2 (1984) 610.

[35] S. Osher, J. A. Sethian, J. Comput. Phys. 79 (1988) 12.

[36] D. Adalsteinsson, J. A. Sethian, J. Comput. Phys. 120 (1995) 128.

[37] E. Dullini, Nucl. Instr. and Meth. B 2 (1984) 610.

[38] M. Kratzer, R. P. Brinkmann, H. Schmidt, G. Wachutka, submitted to J. Appl. Phys.